



TS-1 zeolite encapsulated Pt clusters with enhanced electronic metal-support interaction of Pt–O(H)–Ti for nearly-zero-carbon-emitting photocatalytic hydrogen production from methanol

Shangkun Tian^a, Hongxia Guo^{a,b}, Qiao Zhao^c, Li Liu^{a,b}, Huan Wang^{a,b}, Xiao Wang^{a,b,*}, Sheng Zhang^d, Wenquan Cui^{a,b,*}

^a Hebei Provincial Key Laboratory of Environmental Photocatalytic and Electrocatalytic Materials, College of Chemical Engineering, North China University of Science and Technology, Tangshan 063210, China

^b Hebei Iron and Steel Laboratory, Tangshan 063210, China

^c School of Materials Science and Engineering, National Institute for Advanced Materials, TKL of Metal and Molecule-Based Material Chemistry, Nankai University, Tianjin 300350, China

^d Key Laboratory for Green Chemical Technology of Ministry of Education, Haihe Laboratory of Sustainable Chemical Transformations, School of Chemical Engineering and Technology, Tianjin University, Tianjin 300072, China

ARTICLE INFO

Keywords:

Metal@zeolite
Electronic metal-support interaction
Methanol to hydrogen
Photocatalysis
Zero-carbon emission

ABSTRACT

Photocatalytic H₂ production from methanol is sustainable, yet challenges remain in avoiding carbon-containing gaseous by-products. Titanium silicalite-1 (TS-1) zeolite possesses attractive photocatalytic performance, but lack of modification strategies due to its microporous framework. Herein, we developed a pre-anchoring strategy to confine ultra-small Pt clusters inside TS-1 with ultra-low loading (0.2 mol%), in which Pt were anchored in Ti–OH nests by electronic metal-support interaction (EMSI). The optimal catalyst achieved a remarkable H₂ generation rate of 63.2 mmol g^{−1} h^{−1} in CH₃OH solutions, along with the production of high-value chemical HCHO as the oxidation product with 96.9% selectivity. Investigations reveal that the EMSI between Pt and Ti facilitated the selective decomposition of CH₃OH to H₂ and HCHO, leading to a nearly zero-carbon-emission process. Accordingly, we propose a light-driven carbon-negative "CO₂→CH₃OH→H₂" route, coupling CO₂ utilization and green H₂ production with CH₃OH as the intermediate, therefore offering a new perspective for "liquid sunshine".

1. Introduction

Methanol is an attractive hydrogen carrier owing to its high storage density, enabling safe storage and transportation of H₂ [1]. Considering that harsh reaction conditions are often employed for traditional H₂ production from methanol, photocatalysis offers a clean and sustainable way to drive the on-demand hydrogen production under mild conditions [2]. Research is now focusing on photocatalytic aqueous reforming of methanol, but the primary limitations of this process include the inevitable production of gaseous by-products, specifically CO₂, CO [3] and O₂ [4], which increase the difficulty of product separation and lead to additional carbon emissions. Therefore, it remains challenging to exclude the side reactions and to produce high value-added liquid products, such as formaldehyde (HCHO), during the photocatalytic H₂

production process from CH₃OH.

Generally, the inorganic semiconductor photocatalysts are usually limited by their nonporous and exterior surface properties [5]. On the contrary, the atomically dispersed metal sites in porous materials, such as metal-organic frameworks (MOFs), metal-covalent organic frameworks (M-COFs) and heteroatom-containing zeolites, can be regarded as semiconductor quantum entities or single-site heterogeneous catalysts (SSHC) [6,7]. Among them, Ti-based porous materials, especially titanium silicalite-1 zeolite (TS-1), have attracted increasing attention due to their similar photoredox activity to TiO₂ semiconductor [8–10]. More importantly, unlike the saturated six-coordinated Ti in TiO₂ or Ti-MOFs (such as MIL-125), the atomically dispersed nature of framework Ti sites in TS-1 confers their unique four-coordinated unsaturated electronic environments for optimized adsorption/activation of reactants [11–13].

* Corresponding authors at: Hebei Provincial Key Laboratory of Environmental Photocatalytic and Electrocatalytic Materials, College of Chemical Engineering, North China University of Science and Technology, Tangshan 063210, China.

E-mail addresses: wangxiao@ncst.edu.cn (X. Wang), wqcui@ncst.edu.cn (W. Cui).

<https://doi.org/10.1016/j.apcatb.2024.124201>

Received 29 February 2024; Received in revised form 23 April 2024; Accepted 12 May 2024

Available online 13 May 2024

0926-3373/© 2024 Elsevier B.V. All rights are reserved, including those for text and data mining, AI training, and similar technologies.

In addition, the unique located ligand-to-metal charge-transfer (LMCT) process upon light excitation endows TS-1 with good photocatalytic activity [14–17], and superior selectivity for a certain product [18–20].

However, TS-1 based photocatalysts still suffer from the wide band gap and lack of effective charge transfer pathways. Regrettably, due to its non-alterable crystalline framework and microporous topological structure, very limited modification approaches are currently available for TS-1. Pt is one of the most frequently used photocatalytic co-catalysts for SSHC, and can be either modified on the outer surface to act as traps for photo-generated electrons, or interact with metal nodes directly to modulate the electronic properties [21–23]. However, such a modification strategy via Pt decoration has not yet been applied on TS-1. On one hand, the electrically insulating character of TS-1 zeolite may prevent the transfer of electrons to the metal sites at the outer surface [24]. On the other hand, although zeolite-encapsulated metal (Metal@zeolite) is an attractive class of model catalysts in recent years [25–27], however, compared with pure-silicate and aluminosilicate zeolites [28–30], very limited cases of the successfully encapsulation of metal species inside TS-1 were reported due to its complicated multi-step synthetic procedure. In addition, even if the metal species were successfully encapsulated inside TS-1, it is difficult to guarantee the formation of electronic metal-support interactions (EMSI) between Pt and Ti sites due to their uncontrollable spatial locations. Therefore, improved synthetic strategies are urgently needed to realize the encapsulation of Pt in TS-1 and the formation of EMSI simultaneously.

Herein, we developed a pre-anchoring approach to capture Pt by Ti species via strong electrostatic adsorption (SEA) interaction, therefore successfully prepared a model catalyst with ultra-small Pt clusters encapsulated inside TS-1. Spectroscopic characterizations and electron microscopy results confirm the strong electronic interaction between Pt and Ti sites in the optimal Pt@TS-1(Ti) catalyst, which achieved a remarkable H₂ generation activity in CH₃OH aqueous solutions across a very wide concentration range at room temperature (25 °C), together with a high selectivity of 96.9% towards high-value chemical HCHO. The superior activity and high selectivity of Pt@TS-1(Ti) was revealed by a combination of experimental results and theoretical calculations. According to these strengths, we also propose a light-driven carbon-negative "CO₂→CH₃OH→H₂" route, linking CO₂ utilization with green H₂ production. To the best of our knowledge, this is the first application of Metal@zeolite model catalysts to photocatalysis, therefore broadening their domain of application and providing a viable route for the decoration of heteroatomic zeolites. These findings also provide a powerful new perspective on achieving distributed hydrogen energy utilization and methanol-based economies.

2. Experimental section

2.1. Chemicals

The details of the chemicals and materials used in this study are provided in the [Supplementary material](#).

2.2. Synthesis of TS-1

TS-1 samples were synthesized by hydrothermal method. Tetrabutyl orthotitanate (TBOT, 98%, 0.175 mL) was firstly dissolved in isopropyl alcohol (IPA, 5 mL), and then mixed with tetrapropylammonium hydroxide solution (TPAOH, 2.0 M, 2 mL) and stirred for 0.5 h. In another procedure, TPAOH (2.0 M, 4.4 mL) were added gradually to the tetraethyl orthosilicate (TEOS, 98%, 5 mL) with vigorously stirring for 0.5 h. Subsequently, the above two solutions were mixed and stirred for 5 h, and then heated at 353 K for 30 min to sufficiently remove the ethanol existing in the system and compensated with water. After aged at 373 K for 12 h, the as-obtained mixture was transferred into a PTFE lined autoclave and crystallized at 443 K for 48 h. The sample was cooled to room temperature and the precipitate was separated and

washed with water until pH = 7.5. The recovered solid was dried at 373 K for 12 h and then calcined at 823 K for 6 h.

2.3. Synthesis of xPt@TS-1(Ti)

Pt@TS-1(Ti) samples were synthesized by a pre-anchoring method. Typically, the Pt(en)₂²⁺ ("en" is abbreviation of "NH₂CH₂CH₂NH₂") solution (0.06 M) was first prepared by dissolving 0.16 g of PtCl₂ into 10 mL of an aqueous solution containing 1 mL of ethylenediamine. Then, various amounts of Pt(en)₂²⁺ solution were mixed with TBOT solution (98%, 2 mL) under stirring, and aged at room temperature for 3 h. This step was designed in order to generate some primary structural units to capture Pt(en)₂²⁺. Subsequently, the mixture solution was mixed with TEOS solution (98%, 2 mL) and TPAOH solution (25 wt%, 4.4 mL), with the molar ratio composition of SiO₂: TBOT: TPAOH: H₂O: Pt(en)₂²⁺ = 1: 0.023: 0.579: 9.375: x% (x = 0.01, 0.05, 0.1, 0.2, 0.4 and 0.6). Finally, the mixture solutions were treated and crystallized under hydrothermal conditions similar to that of TS-1, followed by reduction in 10 vol% hydrogen-mixed argon gas at 672 K for 2 h. The obtained samples are named as xPt@TS-1(Ti).

2.4. Synthesis of xPt@TS-1(Si)

The xPt@TS-1(Si) samples were also synthesized by the pre-anchoring method similar to that of xPt@TS-1(Ti), except for that the Pt(en)₂²⁺ solution was firstly mixed with the Si precursor, rather than with Ti precursor. Typically, various amounts of Pt(en)₂²⁺ solution were mixed with TEOS solution (98%, 2 mL) under stirring, followed by the aging procedure. Subsequently, the mixture solution was mixed with the Ti precursor solution and TPAOH, followed by crystallization and H₂ reduction procedures, with the same ratio composition to that of xPt@TS-1(Ti) samples. The obtained samples are named as xPt@TS-1(Si).

2.5. Synthesis of contrast catalysts

Pt@Silicalite-1 (Pt@S-1), Pt/TS-1 and Pt/TiO₂ were prepared as contrast catalysts. The detailed synthesis procedures can be found in the [Supplementary material](#).

2.6. Catalyst characterization

The X-ray diffraction (XRD) patterns were recorded on a Bruker D/max-2500PC diffractometer with a Cu K α radiation (λ =1.5406 Å). Scanning electron microscopy (SEM) images were taken on a Hitachi S-4800 electron microscope. Transmission electron microscopy (TEM) images were obtained on a JEM-2800 F electron microscope at an accelerating voltage of 200 kV. EDX-mapping images in the dark field were acquired to analyze the element distribution. AC-HAADF-STEM images were obtained on a FEI Titan Cubed Themis G2 300 operated at 300 kV. N₂ adsorption/desorption isotherms were measured on a Micromeritics ASAP 2460 analyzer at 77 K after degassed at 573 K for 10 h. The elemental compositions were measured by an inductively coupled plasma optical emission spectrometer (ICP-OES, Perkin-Elmer Optima 5300DV). Ultraviolet-visible diffuse reflectance spectra (UV-vis DRS) were recorded on a Persee TU-1901 UV-vis spectrometer with BaSO₄ as a reference. Fourier transform infrared (FTIR) spectra were recorded on a Bruker Vertex70 spectrometer. Pt L-edge XAFS and Ti K-edge XAFS analyses were performed with Si(111) crystal monochromators at the BL14W Beam line at the Shanghai Synchrotron Radiation Facility (SSRF) (Shanghai, China).

X-ray photoelectron spectra (XPS) were measured by a Thermo ESCALAB 250 Xi instrument with an Al K α (1486.6 eV) monochromatic X-ray source. Fluorescence spectra were measured by a Hitachi F-7000 fluorescence spectrophotometer at an excitation wavelength of 250 nm. Transient state fluorescence spectra were measured on an Edinburgh

Instruments FS5 spectrometer at an excitation wavelength of 250 nm and an emission wavelength of 390 nm. Photoelectrochemical (PEC) measurements were conducted on a Chenhua CHI660E electrochemical workstation with a three-electrode system. *In-situ* diffuse reflection infrared Fourier-transform spectroscopy (DRIFTS) measurements were conducted on a Bruke Tensor II FTIR NEXUS spectrometer, while CO-DRIFTS measurements were performed with CO as the probe molecule on a Bruker Tensor 27 spectrometer. Additional information regarding these measurements can be found in the [Supplementary material](#).

2.7. Catalytic performance test

Before each test, 20 mg catalyst was dispersed in 30 mL of aqueous methanol solution at different concentrations. The reactions were conducted using a photocatalytic H₂ production system (CEL-PAEM-D8plus, Beijing China Education Au-Light Co., Ltd.). The reaction solution was evacuated for 20 min to completely remove the air prior to irradiation under a 500 W mercury lamp. The temperature of the reaction solution was maintained at 298 K using a flow of cooling water during the

reaction. The amount of H₂ produced was analyzed by an on-line gas chromatograph equipped with a TCD detector (GC7920). The solution after the reaction was sampled for formaldehyde detection using UV-visible diffuse reflectance spectroscopy (an acetylacetone method). The amount of formic acid was analyzed by an ion chromatograph (OIC-600), and the amount of other products was analyzed by a gas chromatograph equipped with a FID detector. The efficiency of the photocatalytic reaction was also evaluated in terms of an apparent quantum efficiency (AQE), and the details are provided in the [Supplementary material](#).

2.8. Computational methods

All calculations were based on the density functional theory (DFT) and the details are provided in the [Supplementary material](#).

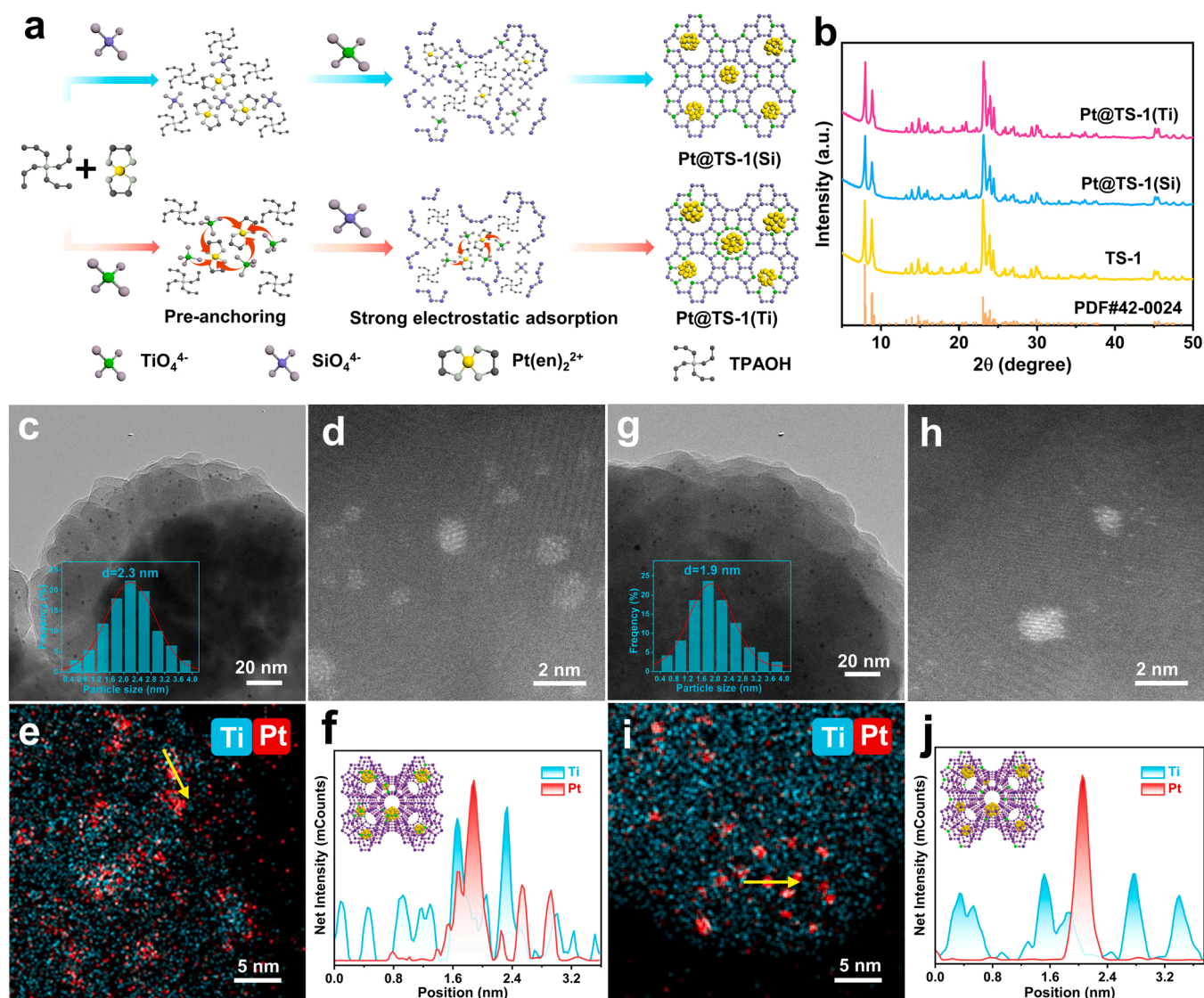


Fig. 1. Synthesis and structural characterizations of Pt@TS-1. (a) Schematic illustration of the preparation of Pt@TS-1 through pre-anchoring strategy. (b) XRD patterns. (c-f) Structural characterizations of Pt@TS-1(Ti), (c) TEM image, the inset is the size distribution of Pt, (d) AC HAADF-STEM image, (e) Elemental mapping image, (f) Extracted line profiles along the yellow arrow in (e), the insert is the schematic structure of Pt@TS-1(Ti). (g-j) Structural characterizations of Pt@TS-1(Si), (g) TEM image, the inset is the size distribution of Pt, (h) AC HAADF-STEM image, (i) Elemental mapping image, (j) Extracted line profiles along the yellow arrow in (i), the insert is the schematic structure of Pt@TS-1(Si).

3. Results and discussion

3.1. Synthesis and characterization of Pt@TS-1

A series of catalysts with Pt clusters confined inside TS-1 zeolites were synthesized via a pre-anchoring strategy. First, ethylenediamine was used to stabilize Pt cations $[\text{Pt}(\text{en})_2]^{2+}$ [31]. Then, we made some modifications to regulate the location and coordination environment of Pt. It is reported that cations could be strongly adsorbed by

deprotonated and negatively charged oxide surfaces via the classic strong electrostatic adsorption (SEA) interaction in an alkaline synthetic environment [32]. Inspired by this, $\text{Pt}(\text{en})_2^{2+}$ complexes were firstly introduced in the initial gel containing Ti precursor or Si precursor, followed by low-temperature aging, in order to generate some primary structural units to capture $\text{Pt}(\text{en})_2^{2+}$. Such a pre-anchoring strategy is illustrated in Fig. 1a (details in Fig. S1).

Taking samples with 0.2 mol% Pt loading as examples, which are abbreviated as Pt@TS-1(Ti) and Pt@TS-1(Si), respectively. The Pt

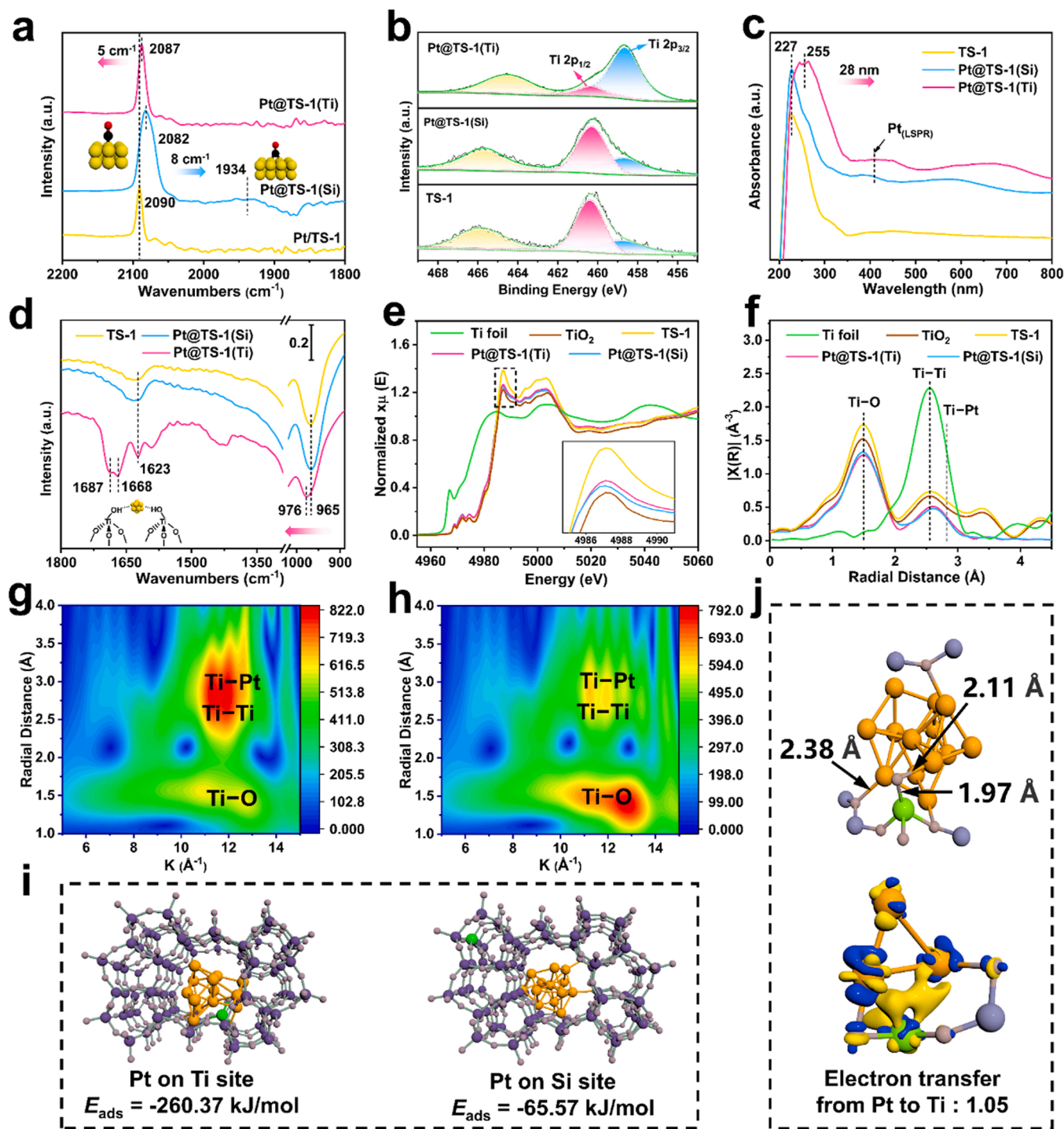


Fig. 2. (a) CO-FTIR. (b) Ti 2p XPS spectra. (c) UV-vis absorption spectra. (d) FTIR spectra. (e) Ti K-edge XANES spectra. (f) Fourier transforms of EXAFS spectra at Ti K-edge. (g) Ti K-edge WT-EXAFS spectra of (g) Pt@TS-1(Ti) and (h) Pt@TS-1(Si), respectively. (i) Calculated adsorption energies of Pt clusters on different sites in Pt@TS-1(Ti). (j) Detailed bond length information and Bader charge analysis for Pt@TS-1(Ti), the orange, green, light purple, and dark purple represent Pt, Ti, O, and Si atoms, respectively; H atoms have been omitted for clarity; yellow and cyan isosurfaces indicate electron accumulation and depletion, respectively.

contents are determined to be 0.33 wt% and 0.35 wt%, respectively (Table S1). The XRD patterns indicate the successful synthesis of TS-1 (Fig. 1b). No characteristic diffraction peaks belonging to Pt species were observed, suggesting the low loading and high dispersion of Pt clusters. The SEM images suggest that both Pt@TS-1(Ti) and Pt@TS-1(Si) exhibit a typical polycrystalline nanosphere morphology without visible metal nanoparticles (Fig. S3-S4). The TEM and element mapping images reveal the highly dispersed Pt clusters in zeolites (Figs. 1c, 1g and Fig. S5-S8). In particular, most Pt clusters are located inside the inner region of TS-1, while the shell of TS-1 is almost empty of metal clusters, as shown in the dark-field scanning TEM images (Fig. S7). In addition, the Pt 4f XPS spectra (Fig. S9) and scanning electron microscopic images under secondary electron mode (Fig. S10) can also reveal that no Pt species on the surface layers [33,34]. All the above results confirm the successful confinement of Pt clusters inside TS-1. In contrast, in Pt/TS-1 samples synthesized without the SEA strategy or by photodeposition method, the majority of Pt particles are on the outer surface of TS-1 (Fig. S11-S12), demonstrating the importance of pre-anchoring strategy to encapsulate Pt into TS-1.

By analyzing more than 200 clusters, the average size of the Pt clusters is 2.3 nm in Pt@TS-1(Ti), while that is 1.9 nm in Pt@TS-1(Si). Notably, the sizes of Pt clusters are much larger than the micropore sizes of TS-1 (~0.55 nm), indicating a collapse of neighboring micropores upon particle growth [35]. The N₂ adsorption-desorption isotherms and pore size distribution curves of Pt@TS-1 samples are shown in Fig. S13, and the textural properties are summarized in Table S2. Compared with the pristine TS-1, very slight decrease of BET surface areas can be observed for Pt@TS-1, indicating that the loading of Pt led to a minimal loss of porosity.

Pt@TS-1(Ti) and Pt@TS-1(Si) were further characterized by aberration-corrected HADDF-STEM imaging. The bright dots are assigned to Pt clusters and no isolated single-atom Pt was observed in these two samples (Figs. 1d and 1h). Elemental mapping images are provided, which show drastically different local atomic environments. In Pt@TS-1(Ti), it can be clearly observed that Ti elements closely scatter around Pt clusters (Fig. 1e). Atomic line profiles were obtained along the selected lines, and Fig. 1f shows the close dispersion of Ti surrounding Pt with a distance <0.5 nm. Such a short intersite distance allows a strong interaction between Pt and Ti [36]. However, in Pt@TS-1(Si) sample, it seems that Ti elements are homogeneously distributed in the TS-1 matrix, rather than around Pt clusters (Figs. 1i and 1j), indicating the absence of such an interaction.

CO was used as a probe molecule for IR spectroscopy to investigate the local environment state of Pt species (Fig. 2a). The peak ascribed to CO linear adsorption over Pt@TS-1(Ti) blue-shifted compared with that over Pt@TS-1(Si), suggesting a higher electron donor capacity of Pt in the former, which is likely due to the formation of interactions between Pt and Ti [37]. In the Ti 2p XPS spectra (Fig. 2b), the peak at 460.4 eV is assigned to the four-coordinated framework Ti [20]. However, this peak for Pt@TS-1(Ti) significantly shifted toward lower binding energy (458.7 eV), suggesting an increased electron density or an increased coordination number in Ti sites [38]. Notably, the highly consistent spectroscopic characterization results for Pt@TS-1(Ti) after an acidic wash (Fig. S14) and the absence of extra-framework TiO₂ peaks at 320 nm in the UV-vis absorption spectra (Fig. 2c) jointly demonstrate the absence of extra-framework Ti [39]. Therefore, it can be speculated that Ti still exists in the form of Si–O–Ti framework, and the termini of which may be opened to form Ti–OH to stabilize Pt clusters, as indicated by Fourier-transform infrared (FTIR) spectra (Fig. 2d and supplementary discussions for Fig. S15) [40].

X-ray absorption spectroscopy measurements were performed to identify the fine structure of the catalysts. The Pt L₃-edge XANES spectra and EXAFS spectra suggest that the Pt species in Pt@TS-1 samples are mainly in metallic state, but slightly tend to high valence states (details in Fig. S16). The average coordination numbers (CNs) of Pt–Pt are lower than 12 of Pt foil, and those of Pt–O are close to 1.0 (Table S3). These

results are consistent with the FT-IR results that metallic Pt clusters are stabilized by defective hydroxyls in the TS-1 framework. As shown in Fig. 2e, the Ti K-edge XANES white line peak of Pt@TS-1(Ti) is close to TiO₂, while that of Pt@TS-1(Si) is close to TS-1. The Ti EXAFS fitting data (Table S4) also show the similar trend, that the CNs of Ti–O in Pt@TS-1(Ti) are 5.5 (close to 6 for TiO₂), demonstrating the formation of opened Ti–OH to stabilize Pt, while those of Pt@TS-1(Si) are 4.8 (close to 4 for TS-1). In the EXAFS spectra (Fig. 2f), the peaks which are assigned to Ti–Ti and Pt–Ti are located at 2.5 Å and 2.7 Å, respectively, making them indistinguishable. Therefore, the wavelet transform (WT) analysis was performed (Fig. 2g-h) to reveal the interaction between Pt and Ti more intuitively. The WT contour plot of Pt@TS-1(Si) displayed only one intensity maximum assigned to the Ti–O coordination. However, the WT signals related to Ti–Ti and Ti–Pt contributions were obviously detected in Pt@TS-1(Ti), indicating the enrichment of Ti surrounding Pt and the formation of strong interaction.

To model the location of Pt clusters in TS-1, the adsorption energies of Pt (Pt₁₃ model) on several potential adsorption sites were calculated (details in Fig. S17). The results suggest that the Pt clusters can be strongly adsorbed by Ti sites (the lowest E_{ads} of $-260.37 \text{ kJ mol}^{-1}$, T1 location in the 10-membered ring) than Si sites (the lowest E_{ads} of $-65.57 \text{ kJ mol}^{-1}$), as shown in Fig. 2i. In addition, Pt is found to be well stabilized by the oxygen atoms in Ti–OH, and the bond distance of Ti–O was stretched to 1.95 Å from 1.84 Å (Fig. 2j), which is in close agreement with the fitting results for the EXAFS data (1.95 Å, Table S4). These results demonstrate the strong anchoring effect of framework Ti for Pt clusters. It is reported that Pt is highly mobile on the abundant hydroxylated silicon surface inside the zeolite channel [41]. Therefore, it is essential to anchor Pt to avoid the migration and agglomeration during synthetic procedures and reactions. Besides, according to Bader charge analysis, the amount of electron transfer from Pt to Ti is 1.05 (Fig. 2j).

We summarized the recent progress in the development of Metal@zeolite catalysts in Table S5. The results suggest that compared with pure silicate or aluminosilicate zeolites, it is difficult to construct single-atomic or sub-nanometric metal sites in TS-1. For example, ultrafine Pt@S-1 can be easily synthesized in our experiments (Fig. S18), but the average size of Pt in Pt@TS-1(Ti) in this work is 2.3 nm, slightly larger than sub-nanometer level. This is attributed to the anchoring effect of Ti to Pt. Due to the relatively low content of framework Ti (one Ti atom per unit cell, i.e., a 96 T cluster model of Si₉₅Ti₁O₁₉₂), a single Ti site may have a limited role in stabilizing Pt, but the enriched Ti sites may be favorable for anchoring a larger Pt cluster. In addition, the formation of EMSI between Pt and Ti would be much more important than simply reducing the particle size of Pt, as discussed below.

3.2. Performance of Pt@TS-1 in photocatalytic H₂ production

The performance of various catalysts was evaluated by photocatalytic H₂ production from methanol aqueous solution. The optimal loading of 0.2 mol% was verified (Fig. S19). Such a low loading of Pt undoubtedly can reduce the cost of catalysts. Fig. 3a represents the mass-specific H₂ generation rates achieved on each catalyst in aqueous methanol (50% by volume) at 25 °C. Pt@TS-1(Ti) exhibits an extremely promoted H₂ yield over pristine TS-1 and contrast catalysts like Pt@TS-1(Si), Pt/TS-1 and Pt/TiO₂, indicating the tremendous effect of interactions between Pt and Ti on reaction outcome. Next, the oxidation product distribution was compared in Fig. 3b. HCHO is the main oxidation product with the selectivity of 96.9% over Pt@TS-1(Ti), along with a trace amount of CO (0.1%), CO₂ (1.2%) and O₂ (1.8%). An electron balance between the reduction products and the oxidation products was almost acquired in this reaction (Fig. S20). This can protect Pt from CO poisoning, and avoid the explosion hazard of H₂/O₂ mixed gas. More importantly, this suggests a potential nearly zero-carbon-emitted H₂ production process coupling with the production of high-value chemical HCHO with high selectivity. In contrast, the selectivity to HCHO dramatically decreased over Pt@TS-1, Pt/TS-1 and Pt/TiO₂,

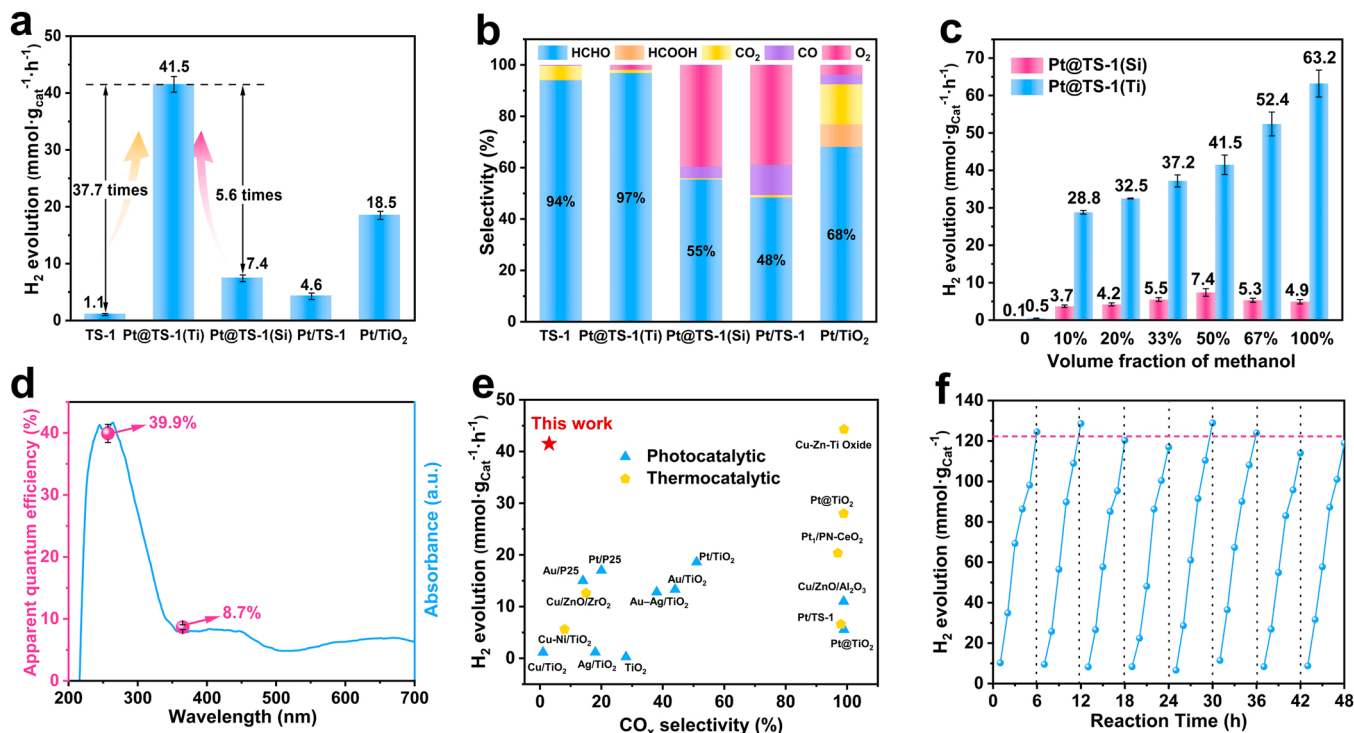


Fig. 3. Performance of Pt@TS-1(Ti) catalyst in photocatalytic H₂ production from methanol. (a) H₂ production rates and (b) Product distributions over Pt@TS-1(Ti) and reference catalysts, reaction conditions: T = 25 °C, 20 mg of catalyst, 30 mL of 50 vol% aqueous methanol solution, 500 W mercury lamp irradiation. (c) H₂ production rates over Pt@TS-1(Ti) and Pt@TS-1(Si) in different proportion of CH₃OH solution. (d) Apparent quantum efficiency of Pt@TS-1(Ti) at different wavelengths. (e) Comparison of photocatalytic H₂ production rates of representative photo- and thermal- catalysts reported in the literature. (f) Cycling stability test of Pt@TS-1(Ti). Error bars represent the means \pm s.d. of three independent experiments.

along with the formation of a large amount of by-products including HCOOH, CO_x and O₂. The findings suggest that significant side reactions occurred on the contrast catalysts, including methanol reforming reaction ($\text{CH}_3\text{OH} + \text{H}_2\text{O} \rightarrow \text{CO}_x + \text{H}_2$), excessive oxidation of CH₃OH [3], and water oxidation, which is likely attributable to the presence of heterogeneous reactive sites.

The performance of the optimal Pt@TS-1(Ti) under different reaction conditions were investigated. Fig. S21 shows the further increased H₂ generation rate along with increasing reaction temperature to 60 °C (112.7 mmol g⁻¹ h⁻¹), indicating its photothermal catalysis capacity. Higher reaction temperatures defy the original intention of photocatalysis with low energy consumption, therefore were not investigated in our work. Fig. 3c shows the performance of Pt@TS-1(Ti) in different proportion of CH₃OH solution at 25 °C. Except for the negligible capability for water-splitting, Pt@TS-1(Ti) exhibits remarkable H₂ generation capability over a wide CH₃OH concentration range, and achieved the highest performance in pure CH₃OH (63.2 mmol g⁻¹ h⁻¹). It is known that the industrial-scale methanol production varies considerably in concentration. For example, the CO₂ per-pass conversion ranges from 35% to 45% in Lurgi process, and the obtained crude CH₃OH contains 30–40 wt% H₂O, while that obtained from the syngas-based process contains 10–12 wt% H₂O [42], leading to the requirement of high energy consumption for purification. Therefore, this great flexibility of Pt@TS-1(Ti) to CH₃OH concentration makes it applicable for unpurified crude CH₃OH, and also resistant to concentration change during the reaction, which is suitable for distributed on-site H₂ production. Besides, this observation strongly suggests that CH₃OH is the predominant reactant and H₂ source over Pt@TS-1(Ti). On the contrary, the most significant activity observed over Pt@TS-1(Si) occurred in the 50 vol% CH₃OH aqueous solution, indicating potential involvement of both H₂O and CH₃OH in the reaction as potential sources of H₂. Besides, the optimum catalyst was applied to other commonly used sacrificial agents (Fig. S22). The results indicate that only those molecules with small

dynamics radius can be effectively applied for H₂ evolution, demonstrating that Pt clusters were successfully encapsulated inside TS-1.

The performance of Pt@TS-1(Ti) were evaluated comprehensively by multiple parameters. Compared with previously reported TS-1 based photocatalysts that can only be performed under ultraviolet light [14–16,20], Pt@TS-1(Ti) exhibits an improved performance under near-visible light irradiation. As shown in Fig. 3d, Pt@TS-1(Ti) achieved a state-of-the-art apparent quantum efficiency (AQE) of 39.9% at 254 nm, and remained at 8.7% at 365 nm. This improved capability of harvesting visible light is attributed to the Pt modification, which is discussed subsequently. The activity of Pt@TS-1(Ti) was compared with reported efficient catalysts for H₂ production from methanol by both photocatalysis and thermal catalysis (Fig. 3e). The comparison reveals that Pt@TS-1(Ti) represents a remarkably higher H₂ generation rate than previously reported photocatalysts, and can even comparable to some of the thermal catalysts (such as Cu-Zn-Ti, operated at 150 °C and under 6 MPa) [43]. More importantly, in contrast with thermal catalysis systems where CO_x are the major oxidation products, the Pt@TS-1(Ti) photocatalyst shows a significant advantage in inhibiting carbon emission (details in Table S6). Finally, the stability of Pt@TS-1(Ti) was tested, implying a steady activity over 48 h (Fig. 3f). The SEM images, XRD patterns and spectroscopic characterizations (Fig. S23–S24) show that the Pt@TS-1(Ti) was still unchanged after the reaction, confirming the superior stability, which is attributed to the intrinsic stability of zeolite and the confinement effect for Pt clusters.

3.3. Promoting effect of EMSI between Pt and Ti on photoelectrical properties

As described previously, Pt@TS-1(Ti) with strong EMSI exhibits extended absorption in the visible light region (Fig. 2c). However, except for the contribution of Pt local surface plasmon resonance (LSPR) at 450 nm [44], the characteristic adsorption peak of TS-1 was also

extended from the UV region to the visible region with an absorption edge of ~ 360 nm, very close to that of TiO_2 semiconductor (~ 380 nm). According to the corresponding Tauc plots (Fig. 4a), Pt@TS-1(Ti) shows a reduced optical bandgap of 3.61 eV compared to that of pristine TS-1 (4.35 eV) and Pt@TS-1(Si) (4.02 eV), which is very close to that of commercial anatase TiO_2 (3.29 eV), indicating the enhanced optical absorption by the formation of EMSI with Pt.

Time-dependent density functional theory (TD-DFT) was carried out to better understand the influence of EMSI on photophysical properties. In Table S7, it is observed that the electron density of the highest occupied molecular orbital (HOMO) and the lowest unoccupied molecular orbital (LUMO) is mainly localized on the O atoms and Ti atoms in TS-1, respectively, indicating the ligand-to-metal charge-transfer (LMCT) process [14]. In Pt@TS-1(Ti), the HOMO and LUMO are localized on Pt atoms and Ti atoms, respectively, indicating the transfer pathway of photo-generated electrons from Pt to Ti under photo-excitation. According to the calculation results, the dominant

excited state of Pt@TS-1(Ti) is mainly contributed by HOMO-10 \rightarrow LUMO+2 configuration. Fig. 4b and Fig. S26 give the contour surfaces of the frontier orbitals associated with this excited state and the results of the Bader charge analysis, respectively, in which visually shows the Pt \rightarrow O(H) \rightarrow Ti pathway, indicating a unique metal-to-ligand-to-metal charge-transfer (MLMCT) process [45]. The same conclusion could also be drawn from the total density of states (TDOS) and partial density of states (PDOS) of Pt@TS-1(Ti). As shown in Fig. 4c and Fig. S27, Pt contributes both to HOMO and LUMO, narrowing the bandgap and leading to the zero-bandgap metallicity of local sites. Therefore, the photo-excitation process in Pt@TS-1(Ti) was dominated by the Pt interband excitation, followed by the charge transfer to Ti via the unique MLMCT pathway. Taken together, Pt decoration in TS-1 significantly enhances the photochemical properties through Pt interband excitation, generating high-energetic electrons and altering the electron transfer pathway, as illustrated in Fig. 4d. Besides, the TDOS analysis also suggests the elevated d -band center of Pt@TS-1(Ti) (-2.30 eV) than that of

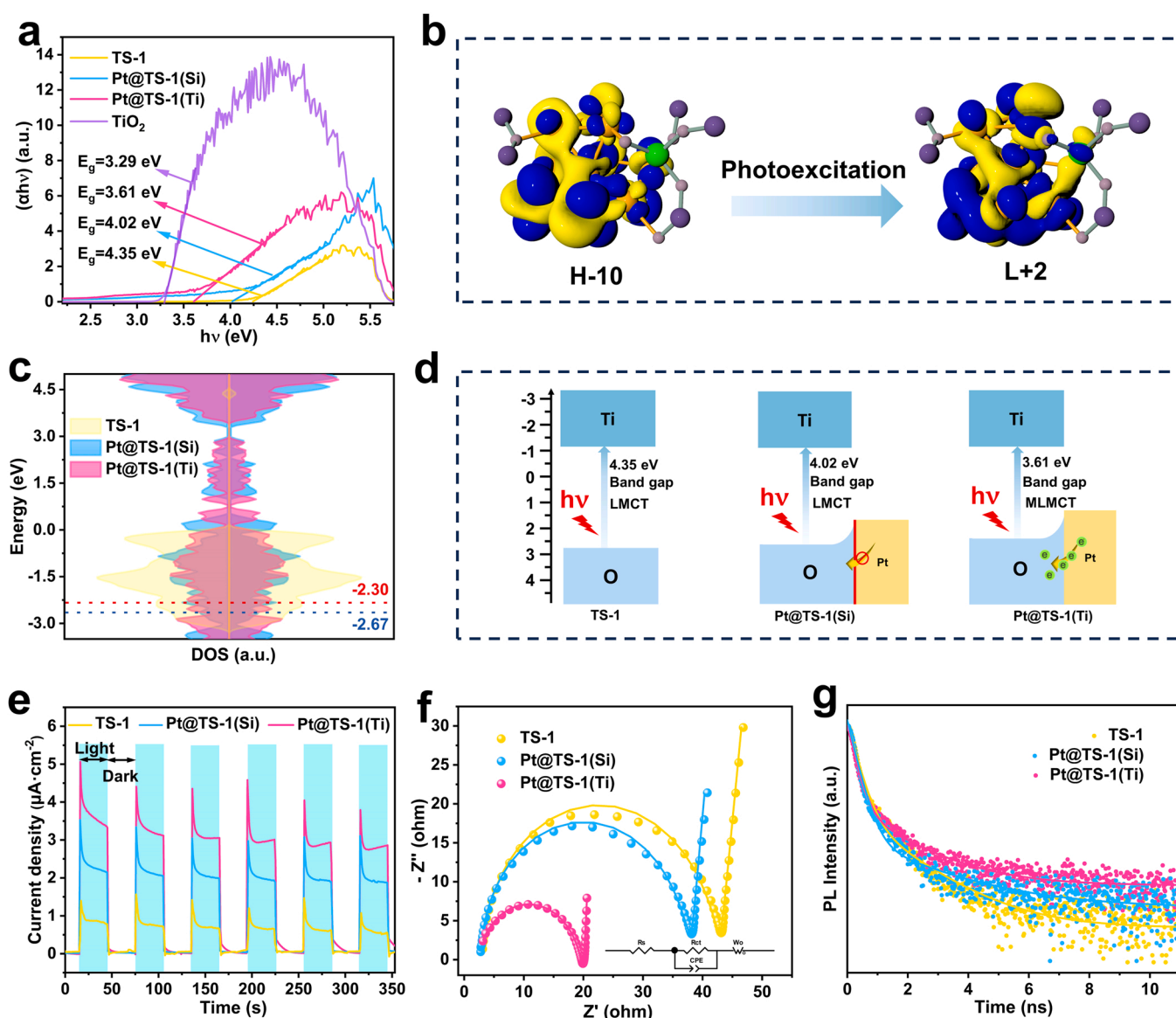


Fig. 4. Photoelectrochemical characterizations of Pt@TS-1(Ti) and reference catalysts. (a) Bandgap energy calculated by the Tauc plots. (b) TD-DFT calculated electronic transition of Pt@TS-1(Ti), the orange, green, light purple, and dark purple represent Pt, Ti, O, and Si atoms, respectively; H atoms have been omitted for clarity; yellow and cyan isosurfaces indicate electron accumulation and depletion, respectively. (c) Total DOS and calculated d -band center. (d) Schematic illustration of band diagrams and electron transfer pathways in pristine TS-1, Pt@TS-1(Si), and Pt@TS-1(Ti), respectively. (e) Photocurrent responses. (f) EIS Nyquist plots. (g) Time-resolved PL spectra.

Pt@TS-1(Si) (-2.67 eV), suggesting the higher adsorption energy towards CH_3OH [46], which is discussed later.

Except for the enhanced photoexcitation properties, it is speculated that the charge dynamics can also be promoted, benefiting from the separation and migration of photo-generated carriers via $\text{Pt} \rightarrow \text{O}(\text{H}) \rightarrow \text{Ti}$ MLMCT pathway. The highest photocurrent density can be observed on the photocurrent response curve of Pt@TS-1(Ti) (Fig. 4e), suggesting the most promoted photocarriers separation and migration efficiency. Electrochemical impedance spectroscopy (EIS) plots (Fig. 4f) show the smallest radius of Pt@TS-1(Ti), indicating its smallest resistance for interfacial charge transfer, consistent with the fitting results (Table S8). Furthermore, electron transfer under light irradiation was investigated through steady-state and time-resolved fluorescence spectroscopy. The significantly quenched fluorescence was observed for Pt@TS-1(Ti) (Fig. S28), indicating the more efficient electron transfer. In Fig. 4g and Table S9, the fluorescence lifetimes of Pt@TS-1(Ti) are much higher than those of pristine TS-1 and Pt@TS-1(Si), indicating the suppressed e^-h^+ recombination. The traditional view is that metal cocatalyst

functions as a trap for photogenerated electrons to facilitate charge separation [23,47]. However, the promoting role of Pt in TS-1 is not attributed to such a Schottky junction formed between metal and substrate, but to the Pt-Ti interaction and the MLMCT carrier transfer scheme, therefore, the photo-generated carriers can be further spatially separated.

3.4. Reaction mechanism study of Pt@TS-1 photocatalysts

The product distribution results (Fig. 3b) indicate the drastically distinct reactions occurred over Pt@TS-1(Ti) compared with other catalysts, which is induced by its unique electronic environment. *In-situ* diffuse reflectance infrared Fourier transform spectra (*in-situ* DRIFTS) were conducted to investigate the reaction intermediates. Fig. 5a shows the spectra over time before and after light irradiation obtained for Pt@TS-1(Ti), and the positions of the main peaks and corresponding groups are summarized in Table S10. Under dark condition, Pt@TS-1(Ti) shows a sharp $\text{Ti}^{4+}-\text{OH}$ peak at 3627 cm^{-1} and $\text{Si}-\text{OH}$ peak at

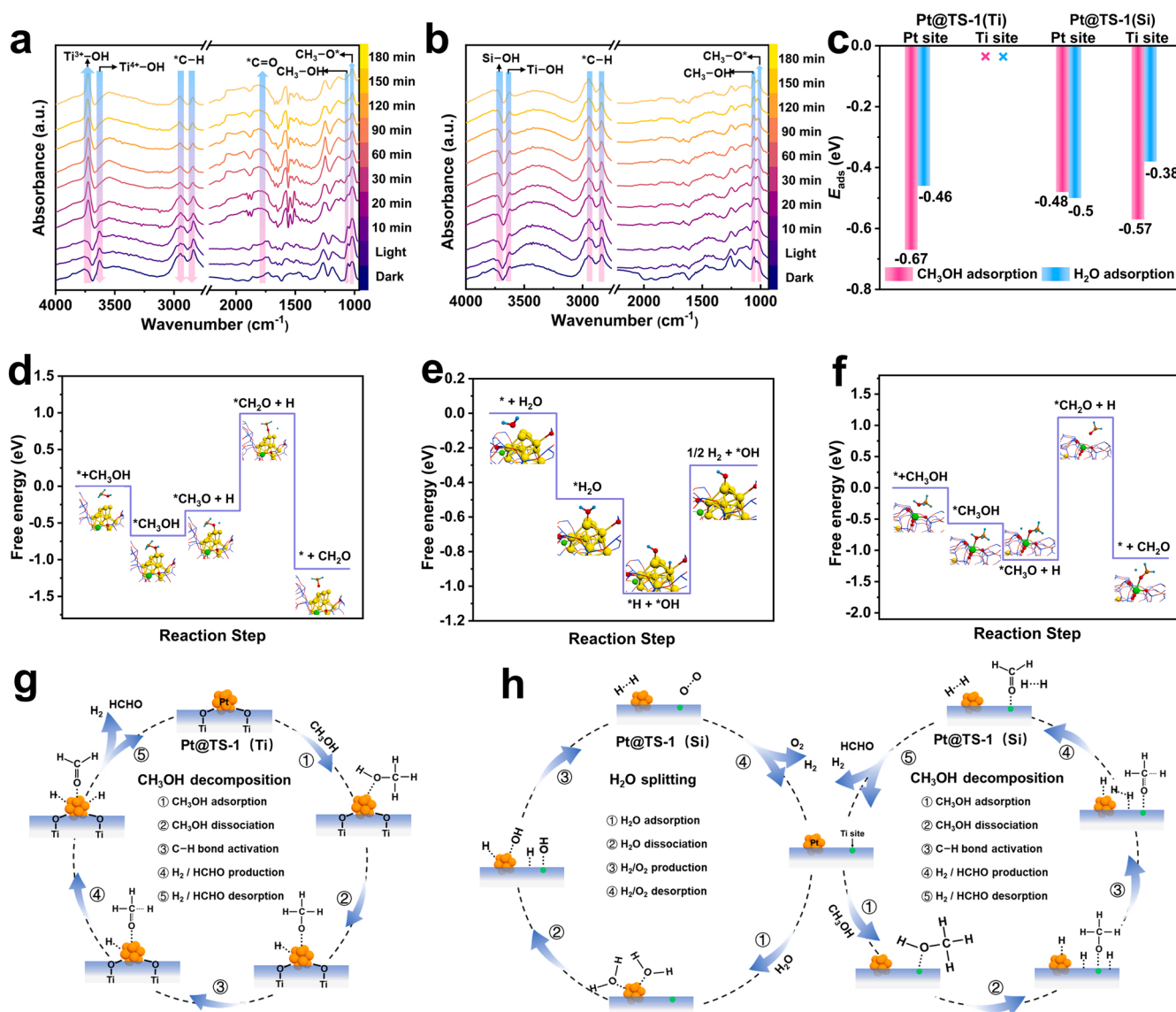


Fig. 5. Mechanism investigation on the catalytic activity. *In-situ* DRIFTS spectra of photocatalytic H_2 evolution on (a) Pt@TS-1(Ti) and (b) Pt@TS-1(Si), respectively. (c) Calculated adsorption energies of reactants on different sites. (d) Gibbs free energy diagram of CH_3OH decomposition on Pt sites in Pt@TS-1(Ti). (e) Gibbs free energy diagram of H_2O splitting on Pt sites and (f) CH_3OH decomposition on Ti sites in Pt@TS-1(Si), respectively. Schematic illustration for the reaction mechanism over (g) Pt@TS-1(Ti) and (h) Pt@TS-1(Si), respectively.

3726 cm^{-1} . After the introduction of light, the $\text{Ti}^{4+}\text{-OH}$ peak completely disappeared, and the sharp $\text{Ti}^{3+}\text{-OH}$ peaks appeared at 3722 cm^{-1} , which is derived from the photoexcitation process in which photogenerated electrons transfer to Ti sites [48]. This demonstrates the $\text{Pt}\rightarrow\text{O}(\text{H})\rightarrow\text{Ti}$ MLMCT photoexcitation in $\text{Pt@TS-1}(\text{Ti})$, consistent with the calculation results. In contrast, the $\text{Ti}^{4+}\text{-OH}$ peak intensities remained unchanged over $\text{Pt@TS-1}(\text{Si})$ with light irradiation, and the $\text{Ti}^{3+}\text{-OH}$ peaks were not observed (Fig. 5b).

The reaction pathways were further investigated. As shown in Fig. 5a, $\text{Pt@TS-1}(\text{Ti})$ exhibited strong CH_3OH adsorption peaks under dark condition (peaks of C-H at 2947 cm^{-1} and 2839 cm^{-1}), while the H_2O adsorption was not obvious (broad band around 3500 cm^{-1}). Under the light illumination, the amount of the adsorbed CH_3OH species decreased. Meanwhile, the upward peaks at 1950 cm^{-1} (produced CH_2O^*) and 1720 cm^{-1} (vC=O) suggest the increased generation of major HCHO products. This can also be evidenced by the downward peaks at 1057 cm^{-1} and 1020 cm^{-1} (vC-O in methoxy) with prolonged light irradiation. The above results clearly demonstrate the conversion of CH_3OH to HCHO , while H_2O did not participate in the reaction. In contrast, $\text{Pt@TS-1}(\text{Si})$ displayed both strong adsorption peaks for H_2O (Fig. 5b, broad band around 3500 cm^{-1}) and CH_3OH (2947 cm^{-1} and 2839 cm^{-1}). However, the almost unchanged peak intensities of the adsorbed species suggest its low activity.

Density functional theory (DFT) calculations were performed to obtain full understanding of reaction mechanism. The four-coordinated Ti sites in TS-1 with and without the anchor of Pt clusters were established, to model the potential catalytic sites in $\text{Pt@TS-1}(\text{Ti})$ and $\text{Pt@TS-1}(\text{Si})$, respectively. The adsorption energies for reactants on different sites are compared in Fig. 5c, and the adsorbed structures are provided in Fig. S29. In $\text{Pt@TS-1}(\text{Ti})$, Pt exhibits an outstanding ability to adsorb CH_3OH (-0.67 eV) than H_2O (-0.46 eV), consistent with the *in-situ* DRIFTS results (Fig. 5a). This superior adsorption capacity is derived from the higher *d*-band center of Pt in $\text{Pt@TS-1}(\text{Ti})$ (Figs. 4c, -2.30 eV, closer to the Fermi-level) than that in $\text{Pt@TS-1}(\text{Si})$ (-2.67 eV), as well as the increased electrophilic property by the electron transfer to Ti, resulting in a strong intermolecular interaction force towards the O atoms in CH_3OH [46,49]. The Gibbs free energy diagrams (Fig. 5d) show the energy barrier of each step for H_2 generation from CH_3OH on Pt sites in $\text{Pt@TS-1}(\text{Ti})$. CH_3OH is initially dehydrogenated into CH_3O^* (the barrier is only 0.34 eV), followed by decomposition into CH_2O^* through C-H bond activation (the barrier is 1.32 eV). Benefiting from the higher-lying *d*-band center, the adsorption of $^*\text{H}$ is enhanced, leading to the formation of final products H_2 and HCHO , which can be easily released from the surface as demonstrated by the LSV curves (Fig. S30). The above mechanism is illustrated in Fig. 5g. Besides, due to the relatively weak adsorption of H_2O and the imbalance in adsorption/desorption energy barrier of H^* , H_2 generation from H_2O is unlikely to occur (details in Fig. S31).

In sharp contrast, as shown in Fig. 5c, CH_3OH and H_2O are preferentially adsorbed on Ti and Pt sites in $\text{Pt@TS-1}(\text{Si})$, respectively, consistent with the *in-situ* DRIFTS results (Fig. 5b). As shown in Fig. 5f, although the first dehydrogenation step of CH_3OH to CH_3O^* is favorable (-0.58 eV), however, the second dehydrogenation step of CH_3O^* to CH_2O^* is energetically too costly (2.28 eV) compared to that over $\text{Pt@TS-1}(\text{Ti})$ (1.32 eV). This result is in great agreement with the *in-situ* DRIFTS results that the adsorbed CH_3O^* species were hardly consumed (Fig. 5b). Besides, water splitting ($\text{H}_2\text{O}^* \rightarrow \text{OH}^* + \text{H}^*$) is thermodynamically favorable on $\text{Pt@TS-1}(\text{Si})$ (Fig. 5e and Fig. S32), demonstrating that both methanol and water participate in the reaction over $\text{Pt@TS-1}(\text{Si})$ and act as the H_2 source together, therefore inevitably results in the formation of O_2 byproducts (selectivity of 39.7%, Fig. 3b).

3.5. A light-driven carbon-negative " $\text{CO}_2\rightarrow\text{CH}_3\text{OH}\rightarrow\text{H}_2$ " route

Shih et al. proposed that the excessive CO_2 can be utilized by using green H_2 from solar energy to produce CH_3OH , which is called "liquid

sunshine" (Route I in Fig. 6) [50]. This process efficiently connects the conversion of solar energy into chemical energy and the existing methanol conversion industry, opening up an avenue for future energy systems and "methanol economics". Considering the unique ability of the $\text{Pt@TS-1}(\text{Ti})$ catalyst in H_2 production from methanol, we suggest a possible supplementary route for "liquid sunshine". It is known that CO_2 can also be reduced by H_2O to produce solar fuels such as methanol, which is termed as "artificial photosynthesis" [51]. Nevertheless, the yield of CH_3OH achieved through this method may be insufficient for large-scale methanol conversion following purification, rendering it economically unfeasible. Taken into account the strengthens of the $\text{Pt@TS-1}(\text{Ti})$ catalyst developed in this work, we propose that the crude CH_3OH product can be directly used for H_2 production without purification, as illustrated in Fig. 6, Route II. This approach has the following advantages:

- (1) Boosted efficiency of H_2 generation by using CH_3OH as a feed-stock, compared to pure water splitting.
- (2) High flexibility for unpurified crude CH_3OH and high resistance to concentration changes during the reaction.
- (3) Suitable for distributed on-demand H_2 production.
- (4) Carbon-negative throughout the entire " $\text{CO}_2\rightarrow\text{CH}_3\text{OH}\rightarrow\text{H}_2$ " process.
- (5) Completely solar light-driven.

The feasibility of this approach was investigated under laboratory conditions, resulting in the production of CH_3OH from simulated flue gas (15% CO_2 in N_2) and tandem H_2 production at the rate of 21.4 $\text{mmol g}^{-1} \text{h}^{-1}$. No significant decrease in H_2 yield was observed over a period of three days (details in Fig. S34). Thus, this photochemical carbon-negative " $\text{CO}_2\rightarrow\text{CH}_3\text{OH}\rightarrow\text{H}_2$ " route may serve as a supplement for the existing "liquid sunshine" strategy.

4. Conclusions

In summary, we have reported an efficient pre-anchoring strategy for encapsulating ultra-small Pt clusters inside TS-1. The optimal $\text{Pt@TS-1}(\text{Ti})$ catalyst can effectively catalyze H_2 production from CH_3OH aqueous solutions across a very wide concentration range. This process is nearly zero-carbon emitting. The characterization results reveal a strong electronic interaction between Pt and Ti sites, resulting in the narrower band gap as well as the more effective photoexcitation pathway via the MLMCT process, thus enhancing the light absorption and carrier dynamics. The photoexcited Pt species with more delocalized electron charge and higher-lying *d*-band center can readily induce the decomposition of the preferentially adsorbed CH_3OH to generate H_2 and HCHO with high selectivity. Based on these unique properties, we proposed that CO_2 utilization and green H_2 production can be coupled together, with CH_3OH as the intermediate. Such a light-driven carbon-negative " $\text{CO}_2\rightarrow\text{CH}_3\text{OH}\rightarrow\text{H}_2$ " route can serve as a powerful supplement for the existing "liquid sunshine" route. Besides, this work is the first application of the Metal@zeolite model catalysts to photocatalysis, opening an important avenue for robust catalyst design for on-site H_2 production.

CRedit authorship contribution statement

Wenquan Cui: Project administration, Funding acquisition, Conceptualization. **Qiao Zhao:** Writing – review & editing, Software, Funding acquisition. **Hongxia Guo:** Writing – review & editing. **Shangkun Tian:** Writing – original draft, Data curation, Conceptualization. **Sheng Zhang:** Writing – review & editing, Supervision. **Xiao Wang:** Writing – review & editing, Methodology, Data curation, Conceptualization. **Huan Wang:** Writing – review & editing, Formal analysis. **Li Liu:** Supervision, Conceptualization.

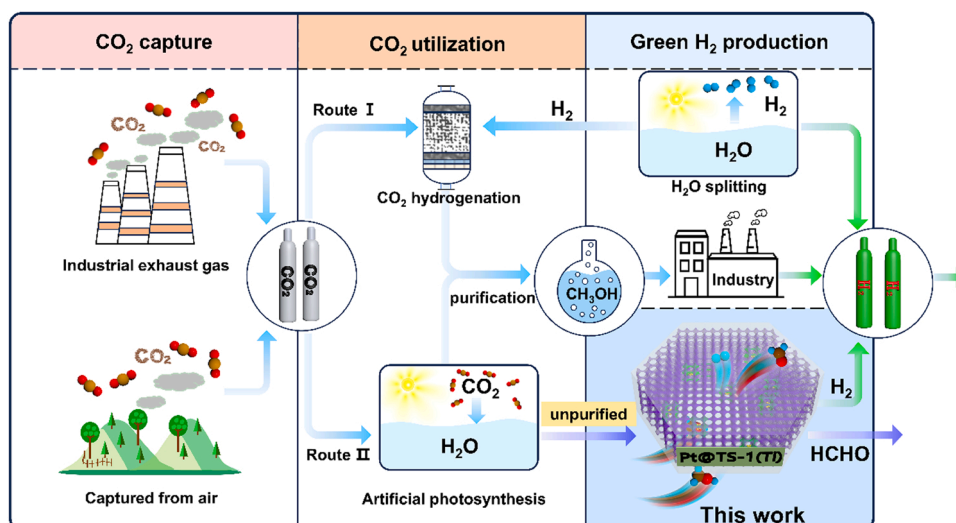


Fig. 6. A light-driven carbon-negative green H_2 production route. Route I, conventional "liquid sunshine" strategy, involves CO_2 capture, H_2 production from renewable energy resources, and the subsequent production of solar CH_3OH by CO_2 hydrogenation under high temperature/pressure conditions. Route II, light-driven " $CO_2 \rightarrow CH_3OH \rightarrow H_2$ " strategy, coupling CO_2 utilization and green H_2 production intermediated via CH_3OH .

Declaration of Competing Interest

The authors declare that they have no known competing financial interests or personal relationships that could have appeared to influence the work reported in this paper.

Data availability

Data will be made available on request.

Acknowledgements

This work was supported by the National Natural Science Foundation of China (Grant No. 22108200 and 22306062); the Key Program of Natural Science Foundation of Hebei Province (Grant No. B2020209017); the Program of Tri-three Talents Project of Hebei Province (Grant No. A202110002); the Natural Science Foundation of Zhejiang Province (Grant No. LQ22B060013); and the Key Program of Talents Project, Tangshan (Grant No. A202301003).

Appendix A. Supporting information

Supplementary data associated with this article can be found in the online version at [doi:10.1016/j.apcatb.2024.124201](https://doi.org/10.1016/j.apcatb.2024.124201).

References

- [1] J. Zhao, R. Shi, Z. Li, C. Zhou, T. Zhang, How to make use of methanol in green catalytic hydrogen production, *Nano Sel.* 1 (2020) 12–29, <https://doi.org/10.1002/nano.202000010>.
- [2] H. Wang, H. Qi, X. Sun, S. Jia, X. Li, T.J. Miao, L. Xiong, S. Wang, X. Zhang, X. Liu, A. Wang, T. Zhang, W. Huang, J. Tang, High quantum efficiency of hydrogen production from methanol aqueous solution with PtCu-TiO₂ photocatalysts, *Nat. Mater.* 22 (2023) 619–626, <https://doi.org/10.1038/s41563-023-01519-y>.
- [3] S. Luo, H. Song, F. Ichihara, M. Oshikiri, W. Lu, D.-M. Tang, S. Li, Y. Li, Y. Li, P. Davin, T. Kako, H. Lin, J. Ye, Light-induced dynamic restructuring of Cu active sites on TiO₂ for low-temperature H_2 production from methanol and water, *J. Am. Chem. Soc.* 145 (2023) 20530–20538, <https://doi.org/10.1021/jacs.3c06688>.
- [4] M. Khan, M.I. Abdullah, A. Samad, Z. Shao, T. Mushiana, A. Akhtar, A. Hameed, N. Zhang, U. Schwingenschlög, M. Ma, Inhibitor and activator: dual role of subsurface sulfide enables selective and efficient electro-oxidation of methanol to formate on CuS@CuO core-shell nanosheet arrays, *Small* 19 (2023) 2205499, <https://doi.org/10.1002/sml.202205499>.
- [5] T. Luo, L. Gilmanova, S. Kaskel, Advances of MOFs and COFs for photocatalytic CO_2 reduction, H_2 evolution and organic redox transformations, *Coord. Chem. Rev.* 490 (2023) 215210, <https://doi.org/10.1016/j.ccr.2023.215210>.
- [6] Y. Xia, M. Sayed, L. Zhang, B. Cheng, J. Yu, Single-atom heterogeneous photocatalysts, *Chem. Catal.* 1 (2021) 1173–1214, <https://doi.org/10.1016/j.checat.2021.08.009>.
- [7] Y. Zhang, H. Liu, F. Gao, X. Tan, Y. Cai, B. Hu, Q. Huang, M. Fang, X. Wang, Application of MOFs and COFs for photocatalysis in CO_2 reduction, H_2 generation, and environmental treatment, *EnergyChem* 4 (2022) 100078, <https://doi.org/10.1016/j.enchem.2022.100078>.
- [8] J. Schneider, M. Matsuoka, M. Takeuchi, J. Zhang, Y. Horiuchi, M. Anpo, D. W. Bahnemann, Understanding TiO₂ photocatalysis: mechanisms and materials, *Chem. Rev.* 114 (2014) 9919–9986, <https://doi.org/10.1021/cr5001892>.
- [9] S.L. Suib, J. Prech, J. Cejka, Y. Kuwahara, K. Mori, H. Yamashita, Some novel porous materials for selective catalytic oxidations, *Mater. Today* 32 (2020) 244–259, <https://doi.org/10.1016/j.mattod.2019.06.008>.
- [10] J. Zhu, P.-Z. Li, W. Guo, Y. Zhao, R. Zou, Titanium-based metal-organic frameworks for photocatalytic applications, *Coord. Chem. Rev.* 359 (2018) 80–101, <https://doi.org/10.1016/j.ccr.2017.12.013>.
- [11] G. Li, N.M. Dimitrijevic, L. Chen, J.M. Nichols, T. Rajh, K.A. Gray, The important role of tetrahedral Ti⁴⁺ sites in the phase transformation and photocatalytic activity of TiO₂ Nanocomposites, *J. Am. Chem. Soc.* 130 (2008) 5402–5403, <https://doi.org/10.1021/ja711118u>.
- [12] Y.-L. Dong, H.-R. Liu, S.-M. Wang, G.-W. Guan, Q.-Y. Yang, Immobilizing isatin-Schiff base complexes in NH₂-UiO-66 for highly photocatalytic CO_2 reduction, *ACS Catal.* 13 (2023) 2547–2554, <https://doi.org/10.1021/acscatal.2c04588>.
- [13] H. Yamashita, K. Mori, Y. Kuwahara, T. Kamegawa, M. Wen, P. Verma, M. Che, Single-site and nano-confined photocatalysts designed in porous materials for environmental uses and solar fuels, *Chem. Soc. Rev.* 47 (2018) 8072–8096, <https://doi.org/10.1039/C8CS00341F>.
- [14] H. Yin, F. Su, C. Luo, L. Zhu, W. Zhong, L. Mao, K. You, D. Yin, Visible-light-mediated remote aliphatic C–H oxyfunctionalization over CuCl₂ decorated hollowed-TS-1 photocatalysts, *Appl. Catal. B: Environ.* 302 (2022) 120851, <https://doi.org/10.1016/j.apcatb.2021.120851>.
- [15] I. Khan, X. Chu, Y. Liu, S. Khan, L. Bai, L. Jing, Synthesis of Ni²⁺ cation modified TS-1 molecular sieve nanosheets as effective photocatalysts for alcohol oxidation and pollutant degradation, *Chin. J. Catal.* 41 (2020) 1589–1602, [https://doi.org/10.1016/S1872-2067\(20\)63555-0](https://doi.org/10.1016/S1872-2067(20)63555-0).
- [16] Z. Zhao, D.-G. Cheng, F. Chen, X. Zhan, Hierarchical porous TS-1/Pd/CdS catalysts for enhanced photocatalytic hydrogen evolution, *Int. J. Hydrog. Energ.* 45 (2020) 33532–33542, <https://doi.org/10.1016/j.ijhydene.2020.09.099>.
- [17] Y. Tong, L. Chen, S. Ning, N. Tong, Z. Zhang, H. Lin, F. Li, X. Wang, Photocatalytic reduction of CO_2 to CO over the Ti-highly dispersed HZSM-5 zeolite containing Fe, *Appl. Catal. B: Environ.* 203 (2017) 725–730, <https://doi.org/10.1016/j.apcatb.2016.10.065>.
- [18] C. Gao, J. Wang, H. Xu, Y. Xiong, Coordination chemistry in the design of heterogeneous photocatalysts, *Chem. Soc. Rev.* 46 (2017) 2799–2823, <https://doi.org/10.1039/C6CS00727A>.
- [19] H. Wang, T. Yang, J. Wang, Z. Zhou, Z. Pei, S. Zhao, Coordination engineering in single-site catalysts: general principles, characterizations, and recent advances, *Chem* 10 (2024) 48–85, <https://doi.org/10.1016/j.chempr.2023.08.014>.
- [20] P. Tao, X. Wang, Q. Zhao, H. Guo, L. Liu, X. Qi, W. Cui, Framework Ti-rich titanium silicalite-1 zeolite nanoplates for enhanced photocatalytic H_2 production from CH_3OH , *Appl. Catal. B: Environ.* 325 (2023) 122392, <https://doi.org/10.1016/j.apcatb.2023.122392>.
- [21] X.-Y. Meng, J.-J. Li, P. Liu, M. Duan, J. Wang, Y.-N. Zhou, Y. Xie, Z.-H. Luo, Y.-X. Pan, Long-term stable hydrogen production from water and lactic acid via

- visible-light-driven photocatalysis in a porous microreactor, *Angew. Chem. Int. Ed.* 62 (2023) e202307490, <https://doi.org/10.1002/anie.202307490>.
- [22] X. Fang, Q. Shang, Y. Wang, L. Jiao, T. Yao, Y. Li, Q. Zhang, Y. Luo, H.-L. Jiang, Single Pt atoms confined into a metal-organic framework for efficient photocatalysis, *Adv. Mater.* 30 (2018) 1705112, <https://doi.org/10.1002/adma.201705112>.
- [23] M. Chen, Z. Ye, L. Wei, J. Yuan, L. Xiao, Shining at the tips: anisotropic deposition of Pt nanoparticles boosting hot carrier utilization for plasmon-driven photocatalysis, *J. Am. Chem. Soc.* 144 (2022) 12842–12849, <https://doi.org/10.1021/jacs.2c04202>.
- [24] T. Wang, Y. Chu, X. Li, Y. Liu, H. Luo, D. Zhou, F. Deng, X. Song, G. Lu, J. Yu, Zeolites as a class of semiconductors for high-performance electrically transduced sensing, *J. Am. Chem. Soc.* 145 (2023) 5342–5352, <https://doi.org/10.1021/jacs.2c13160>.
- [25] Q. Zhang, S. Gao, J. Yu, Metal sites in zeolites: synthesis, characterization, and catalysis, *Chem. Rev.* 123 (2023) 6039–6106, <https://doi.org/10.1021/acs.chemrev.2c00315>.
- [26] Y. Chai, W. Dai, G. Wu, N. Guan, L. Li, Confinement in a zeolite and zeolite catalysis, *Acc. Chem. Res.* 54 (2021) 2894–2904, <https://doi.org/10.1021/accs.accounts.1c00274>.
- [27] Y. Ma, S. Song, C. Liu, L. Liu, L. Zhang, Y. Zhao, X. Wang, H. Xu, Y. Guan, J. Jiang, W. Song, Y. Han, J. Zhang, P. Wu, Germanium-enriched double-four-membered-ring units inducing zeolite-confined subnanometric Pt clusters for efficient propane dehydrogenation, *Nat. Catal.* 6 (2023) 506–518, <https://doi.org/10.1038/s41929-023-00968-7>.
- [28] G. Xu, X. Zhang, Z. Dong, W. Liang, T. Xiao, H. Chen, Y. Ma, Y. Pan, Y. Fu, Ferric single-site catalyst confined in a zeolite framework for propane dehydrogenation, *Angew. Chem. Int. Ed.* 62 (2023) e202305915, <https://doi.org/10.1002/anie.202305915>.
- [29] Q. Cheng, X. Yao, L. Ou, Z. Hu, L. Zheng, G. Li, N. Morlanes, J.L. Cerrillo, P. Castaño, X. Li, J. Gascon, Y. Han, Highly efficient and stable methane dry reforming enabled by a single-site cationic Ni catalyst, *J. Am. Chem. Soc.* 145 (2023) 25109–25119, <https://doi.org/10.1021/jacs.3c04581>.
- [30] W. Shang, B. Qin, M. Gao, X. Qin, Y. Chai, G. Wu, N. Guan, D. Ma, L. Li, Efficient heterogeneous hydroformylation over zeolite-encaged isolated rhodium ions, *CCS Chem.* 5 (2023) 1526–1539, <https://doi.org/10.31635/ccschem.022.202202043>.
- [31] N. Wang, Q. Sun, J. Yu, Ultrasmall metal nanoparticles confined within crystalline nanoporous materials: a fascinating class of nanocatalysts, *Adv. Mater.* 31 (2019) 1803966, <https://doi.org/10.1002/adma.201803966>.
- [32] Y. Wang, S. Qin, N. Denisov, H. Kim, Z. Bad'ura, B.B. Sarma, P. Schmuki, Reactive deposition versus strong electrostatic adsorption (SEA): a key to highly active single atom co-catalysts in photocatalytic H₂ generation, *Adv. Mater.* 35 (2023) 2211814, <https://doi.org/10.1002/adma.202211814>.
- [33] Q. Sun, N. Wang, T. Zhang, R. Bai, A. Mayoral, P. Zhang, Q. Zhang, O. Terasaki, J. Yu, Zeolite-encaged single-atom Rh catalysis: highly-efficient hydrogen generation and shape-selective tandem hydrogenation of nitroarenes, *Angew. Chem. Int. Ed.* 58 (2019) 18570–18576, <https://doi.org/10.1002/anie.201912367>.
- [34] Y. Zeng, J. Liang, C. Li, Z. Qiao, B. Li, S. Hwang, N.N. Kariuki, C.-W. Chang, M. Wang, M. Lyons, S. Lee, Z. Feng, G. Wang, J. Xie, D.A. Cullen, D.J. Myers, G. Wu, Regulating catalytic properties and thermal stability of Pt and PtCo intermetallic fuel-cell catalysts via strong coupling effects between single-metal site-rich carbon and Pt, *J. Am. Chem. Soc.* 145 (2023) 17643–17655, <https://doi.org/10.1021/jacs.3c03345>.
- [35] X. Wei, J. Cheng, Y. Li, K. Cheng, F. Sun, Q. Zhang, Y. Wang, Bimetallic clusters confined inside silicalite-1 for stable propane dehydrogenation, *Nano Res.* 16 (2023) 10881–10889, <https://doi.org/10.1007/s12274-023-5953-y>.
- [36] L. Zeng, Z. Zhao, Q. Huang, C. Zhou, W. Chen, K. Wang, M. Li, F. Lin, H. Luo, Y. Gu, L. Li, S. Zhang, F. Lv, G. Lu, M. Luo, S. Guo, Single-atom Cr–N₄ sites with high oxophilicity interfaced with Pt atomic clusters for practical alkaline hydrogen evolution catalysis, *J. Am. Chem. Soc.* 145 (2023) 21432–21441, <https://doi.org/10.1021/jacs.3c06863>.
- [37] L. Liu, U. Díaz, R. Arenal, G. Agostini, P. Concepción, A. Corma, Generation of subnanometric platinum with high stability during transformation of a 2D zeolite into 3D, *Nat. Mater.* 16 (2017) 132–138, <https://doi.org/10.1038/nmat4757>.
- [38] J. Zhang, H. Shi, Y. Song, W. Xu, X. Meng, J. Li, High-efficiency synthesis of enhanced-titanium and anatase-free TS-1 zeolite by using a crystallization modifier, *Inorg. Chem. Front.* 8 (2021) 3077–3084, <https://doi.org/10.1039/D1QI00311A>.
- [39] J. Tekla, K.A. Tarach, Z. Olejniczak, V. Girmán, K. Góra-Marek, Effective hierarchization of TS-1 and its catalytic performance in cyclohexene epoxidation, *Micro Mesopor. Mat.* 233 (2016) 16–25, <https://doi.org/10.1016/j.micromeso.2016.06.031>.
- [40] J. Zhang, R. Bai, Z. Feng, J. Li, Amide-assisted synthesis of TS-1 zeolites with active Ti(OH)₂(OH)₂(OSi)₂ sites toward efficient oxidative desulfurization, *Appl. Catal. B: Environ.* 342 (2024) 123339, <https://doi.org/10.1016/j.apcatb.2023.123339>.
- [41] H. Wan, L. Qian, N. Gong, H. Hou, X. Dou, L. Zheng, L. Zhang, L. Liu, Size-dependent structures and catalytic properties of supported bimetallic PtSn catalysts for propane dehydrogenation reaction, *ACS Catal.* 13 (2023) 7383–7394, <https://doi.org/10.1021/acscatal.3c00548>.
- [42] J. Zhong, X. Yang, Z. Wu, B. Liang, Y. Huang, T. Zhang, State of the art and perspectives in heterogeneous catalysis of CO₂ hydrogenation to methanol, *Chem. Soc. Rev.* 49 (2020) 1385–1413, <https://doi.org/10.1039/C9CS00614A>.
- [43] Z. Sun, S. Fang, Y. Lin, Y.H. Hu, Photo-assisted methanol steam reforming on solid solution of Cu–Zn–Ti oxide, *Chem. Eng. J.* 375 (2019) 121909, <https://doi.org/10.1016/j.cej.2019.121909>.
- [44] Z.-X. Sun, K. Sun, M.-L. Gao, Ö. Metin, H.-L. Jiang, Optimizing Pt electronic states through formation of a Schottky junction on non-reducible metal-organic frameworks for enhanced photocatalysis, *Angew. Chem. Int. Ed.* 61 (2022) e202206108, <https://doi.org/10.1002/anie.202206108>.
- [45] H. Zhang, S. Si, G. Zhai, Y. Li, Y. Liu, H. Cheng, Z. Wang, P. Wang, Z. Zheng, Y. Dai, T.X. Liu, B. Huang, The long-distance charge transfer process in ferrocene-based MOFs with FeO₆ clusters boosts photocatalytic CO₂ chemical fixation, *Appl. Catal. B: Environ.* 337 (2023) 122909, <https://doi.org/10.1016/j.apcatb.2023.122909>.
- [46] C. Wang, W. Zhang, J. Wang, P. Xia, X. Duan, Q. He, I. Sirés, Z. Ye, Accelerating Fe(III)/Fe(II) redox cycling in heterogeneous electro-Fenton process via S/Cu-mediated electron donor-shuttle regime, *Appl. Catal. B: Environ.* 342 (2024) 123457, <https://doi.org/10.1016/j.apcatb.2023.123457>.
- [47] M. Zhang, X. Wang, X. Qi, H. Guo, L. Liu, Q. Zhao, W. Cui, Effect of Ag cocatalyst on highly selective photocatalytic CO₂ reduction to HCOOH over CuO/Ag/UiO-66 Z-scheme heterojunction, *J. Catal.* 413 (2022) 31–47, <https://doi.org/10.1016/j.jcat.2022.06.014>.
- [48] L. Liu, C. Zhao, J.T. Miller, Y. Li, Mechanistic study of CO₂ photoreduction with H₂O on Cu/TiO₂ nanocomposites by in situ X-ray absorption and infrared spectroscopies, *J. Phys. Chem. C* 121 (2017) 490–499, <https://doi.org/10.1021/acs.jpcc.6b10835>.
- [49] W. Chen, S. Luo, M. Sun, X. Wu, Y. Zhou, Y. Liao, M. Tang, X. Fan, B. Huang, Z. Qian, High-entropy intermetallic PtRhBiSnSb nanoplates for highly efficient alcohol oxidation electrocatalysis, *Adv. Mater.* 34 (2022) 2206276, <https://doi.org/10.1002/adma.202206276>.
- [50] C. Shih, T. Zhang, J. Li, C. Bai, Powering the future with liquid sunshine, *Joule* 2 (2018) 1925–1949, <https://doi.org/10.1016/j.joule.2018.08.016>.
- [51] S. Zhu, Q. Zhao, H. Guo, L. Liu, X. Wang, X. Qi, X. Meng, W. Cui, Construction of a Cu@hollow TS-1 nanoreactor based on a hierarchical full-spectrum solar light utilization strategy for photothermal synergistic artificial photosynthesis, *Carbon Energy* 6 (2024) e499, <https://doi.org/10.1002/cey2.499>.